

Chemical composition in the IRAS 16562–3959 high-mass star-forming region

KOTOMI TANIGUCHI,¹ ANDRÉS E. GUZMÁN,² LITON MAJUMDAR,³ MASAO SAITO,^{2,4} AND KAZUKI TOKUDA^{5,2}

¹*Department of Physics, Faculty of Science, Gakushuin University, Mejiro, Toshima, Tokyo 171-8588, Japan*

²*National Astronomical Observatory of Japan (NAOJ), National Institutes of Natural Sciences, Osawa, Mitaka, Tokyo 181-8588, Japan*

³*School of Earth and Planetary Sciences, National Institute of Science Education and Research, HBNI, Jatni 752050, Odisha, India*

⁴*Department of Astronomical Science, School of Physical Science, SOKENDAI (The Graduate University for Advanced Studies), Osawa, Mitaka, Tokyo 181-8588, Japan*

⁵*Department of Physical Science, Graduate School of Science, Osaka Prefecture University, 1-1 Gakuen-cho, Naka-ku, Sakai, Osaka 599-8531, Japan*

(Received; Revised; Accepted)

Submitted to ApJ

ABSTRACT

We have analyzed the Atacama Large Millimeter/submillimeter Array (ALMA) cycle 2 data of band 6 toward the G345.4938+01.4677 massive young protostellar object (G345.5+1.47 MYSO) in the IRAS 16562–3959 high-mass star-forming region with an angular resolution of $\sim 0''.3$, corresponding to ~ 760 au. We spatially resolve the central region which consists of three prominent molecular emission cores. A hypercompact (HC) H II region (Core A) and two molecule-rich cores (Core B and Core C) are identified using the moment zero images of the H30 α line and a CH₃OH line, respectively. Various oxygen-bearing complex organic molecules (COMs), such as (CH₃)₂CO and CH₃OCHO, have been detected toward the positions of Core B and Core C, while nitrogen-bearing species, CH₃CN, HC₃N and its ¹³C isotopologues, have been detected toward all of the cores. We discuss the formation mechanisms of H₂CO by comparing the spatial distribution of C¹⁸O with that of H₂CO. The ³³SO emission, on the other hand, shows a ring-like structure surrounding Core A, and it peaks on the outer edge of the H30 α emission region. These results imply that SO is enhanced in a shock produced by the expanding motion of the ionized region.

Keywords: astrochemistry – ISM: molecules – stars: massive

1. INTRODUCTION

Complex organic molecules (COMs), consisting of more than six atoms and rich in hydrogen, are abundant in the compact (~ 0.1 pc) dense and hot gas ($n \geq 10^7$ cm⁻³, $T > 100$ K) around massive young protostars (Herbst & van Dishoeck 2009). Their chemistry is known as hot-core chemistry. Development of radio observational facilities has enabled detailed investigation of this chemistry toward high-mass star-forming regions (Bonfand et al. 2019; Gieser et al. 2019; Pagani et al. 2019; Tercero et al. 2018). Well-studied Galactic hot cores are the Sagittarius B2 (e.g., Bonfand et al. 2017, 2019) and the Orion region (e.g., Friedel & Widicus Weaver 2012; Widicus Weaver & Friedel 2012; Feng et al. 2015). Outside the Galaxy, oxygen-bearing COMs (e.g., methanol, methyl formate, and dimethyl ether) have been detected from hot cores in the Large and Small Magellanic Clouds (LMC and SMC) (Sewilo et al. 2019).

The detection in Sgr B2 of iso-propyl cyanide, a branched alkyl molecule, suggested a possible link between the interstellar COMs and pre-biotic molecules such as amino acids detected in meteorites due to their key side chain structure (Belloche et al. 2014). The levels of deuterium fractionation of COMs in Sgr B2 are lower than a prediction by a chemical model (Belloche et al. 2016). Nitrogen-bearing COMs and oxygen-bearing COMs show different spatial distributions in the Orion region (Feng et al. 2015). The chemical diversity around massive young stellar ob-

Table 1. Summary of spectral windows covered by the correlator setup

Frequency ^a (GHz)	Frequency ^a resolution (kHz)	Velocity resolution (km s ⁻¹)	1 σ noise (mJy/beam)
216.976–218.849	1953.1	3.0	1.1
219.533–219.767	488.3	0.8	1.5
220.533–220.767	244.1	0.4	2.0
231.803–232.037	488.3	0.8	2.1

^aObtained from [Cesaroni et al. \(2017\)](#).

jects (MYSOs) were also found; carbon-chain-poor/COMs-rich sources and a carbon-chain-rich/COMs-poor source ([Taniguchi et al. 2017, 2018a,b](#)). These results show that hot core chemistry processes are far from being settled, and detailed observational data from a variety of sources is still needed.

The G345.5+1.47 MYSO ([Mottram et al. 2007](#)) is located in the center of the IRAS 16562–3959 high-mass star-forming region ([Skrutskie et al. 2006](#)). The distance and bolometric luminosity (L_{bol}) are 2.4 kpc and 154400 L_{\odot} ([Lumsden et al. 2013](#)), respectively. In the IRAS 16562–3959 high-mass star-forming region, 18 continuum cores have been detected in ALMA band 3 ([Guzmán et al. 2014](#)). They also detected various sulfur-bearing species such as SO, SO₂, CS, and OCS, and velocity gradients in the first moment maps of the first two. A hot molecular outflow driven by an ionized jet has been detected at the G345.5+1.47 MYSO ([Guzmán et al. 2011](#)). [Cesaroni et al. \(2017\)](#) investigated whether circumstellar rotating disk around the G345.5+1.47 MYSO exists by analyzing the CH₃CN (12 – 11), ¹³CH₃CN (13 – 12), and SiO (5 – 4) rotational transitions using ALMA. Though such disks are ubiquitous in low-mass YSOs, they could not identify it around this high-mass YSO. [Guzmán et al. \(2018\)](#) showed the spatial distributions of several molecules toward the IRAS 16562–3959 by using the ALMA band 3 observations. In this region, [Guzmán et al. \(2018\)](#) suggested the presence of different chemically evolutionary stages, and thus it is crucial to investigate its chemical properties in detail. However, an angular resolution of 1''.7 was not enough to spatially resolve the central G345.5+1.47 MYSO ([Guzmán et al. 2018](#)). It is still unclear whether chemical properties of hot cores in the same region are similar to each other or not, and, if they are different, whether the difference relates to the local physical conditions or not.

In this paper, we present ALMA band 6 data toward the G345.5+1.47 MYSO with a higher spatial resolution of $\sim 0''.3$ (~ 760 au). In Section 2, details about the archival data and reduction procedures are described. The continuum image, moment zero images of several molecular emission lines, and spectra toward three cores which we identify in this paper are presented in Sections 3.1, 3.2, and 3.3, respectively. Analytical methods and results of the spectra are described in Section 3.4. We compare the chemical composition between the two main cores detected in Section 4.1. We discuss relationships of spatial distributions between C¹⁸O and H₂CO, and between ³³SO and H30 α in Sections 4.2 and 4.3, respectively. In Section 5, we summarize the main conclusions of this paper.

2. DATA AND REDUCTION PROCEDURE

We present archival data from cycle 2 data, band 6 (project ID; 2013.1.00489.S, PI; Riccardo Cesaroni). Observational details are given by [Cesaroni et al. \(2017\)](#). Table 1 summarizes the frequency band and resolution of each spectral window. The spectral window with the widest frequency coverage was used for a continuum observation. The field of view (FoV) and largest angular scale (LAS) of the 12 m array observations are $\sim 26''$ and $\sim 4''.4$, respectively. The coordinate of the center of the target source is $(\alpha_{\text{J2000}}, \delta_{\text{J2000}}) = (16^{\text{h}}59^{\text{m}}41^{\text{s}}.61, -40^{\circ}03'43''.3)$. The angular resolutions are approximately $0''.32 \times 0''.25$, corresponding to 768 au \times 600 au at the source distance of 2.4 kpc.

We conducted data reduction and imaging using the Common Astronomy Software Application (CASA v 4.3.1; [McMullin et al. 2007](#)) on the pipeline-calibrated visibilities. The data cubes were imaged with the TCLEAN task within CASA. Natural weighting was applied. Velocity resolutions for each spectral window and the noise levels

attained are given in Table 1. Continuum images were obtained from the data cubes using the IMCONTSUB task. The rms noise level of the continuum image is $1.6 \text{ mJy beam}^{-1}$.

3. RESULTS AND ANALYSES

3.1. Continuum Image and the H_2 Column Density of Identified Cores

Figure 1 shows the continuum image made from the widest spectral window (216.961 – 218.834 GHz, Table 1). The angular resolution is $0''.32 \times 0''.25$. The strongest continuum peak associates with the G345.5+1.47 MYSO, which is indicated as Core A in Figure 1. Another continuum peak corresponds to Core C, which we will identify later in this subsection. A small continuum peak, labeled as D in Figure 1, is detected at the north position from Core A, and a weak continuum emission has been detected at the Core B position.

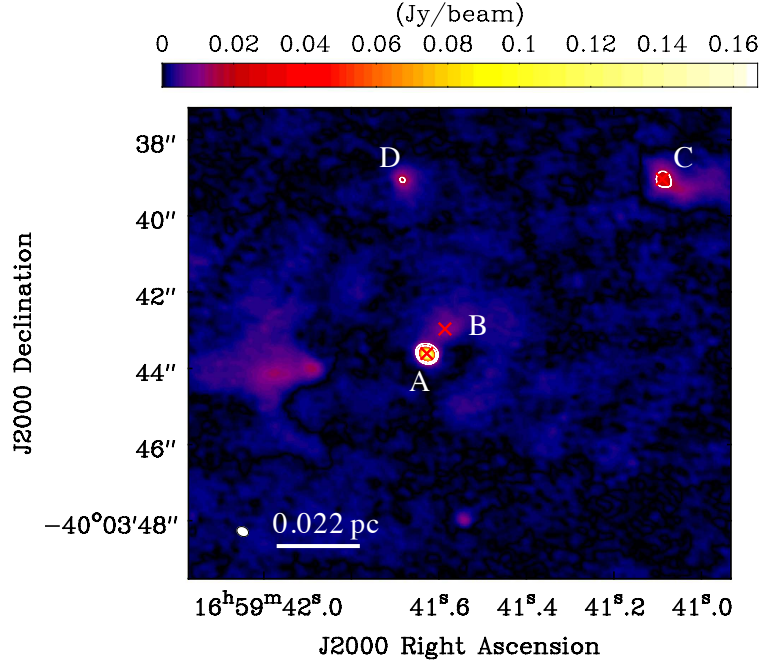


Figure 1. Continuum image made from the 216.961 – 218.834 GHz spectral window. The contour levels are 10% and 20% of the peak intensity ($0.167 \text{ Jy beam}^{-1}$). Red crosses labeled as A – C indicate the positions of cores identified by the $H_{30}\alpha$ and CH_3OH moment zero images (Figure 2). The white ellipse at the left bottom indicates the angular resolution of approximately $0''.32 \times 0''.25$.

We define the position of the hypercompact (HC) H II region and that of prominent molecular emission based on the $H_{30}\alpha$ and CH_3OH ($4_{-2,3} - 3_{-1,2} E$) moment zero maps. These positions are shown in the continuum map (Figure 1) and in the moment zero maps of the $H_{30}\alpha$ and of the methanol transition shown in Figure 2. Core A corresponds to the HCH II region, and Cores B and C correspond to the strongest rich molecular cores identified in IRAS 16562–3959 by Cesaroni et al. (2017) and by Guzmán et al. (2018). Table 2 lists general properties of these cores based on 2D Gaussian fittings to the moment zero maps.

We derived the H_2 column density, N_{H_2} , at each core using the following formula (Kauffmann et al. 2008):

$$N_{H_2} = 2.02 \times 10^{20} \left(e^{1.439(\lambda/\text{mm})^{-1}(T/10\text{K})^{-1}} - 1 \right) \left(\frac{\kappa_\nu}{0.01 \text{ cm}^2 \text{ g}^{-1}} \right)^{-1} \left(\frac{F_\nu^{\text{beam}}}{\text{mJy beam}^{-1}} \right) \left(\frac{\theta_{\text{HPBW}}}{10 \text{ arcsec}} \right)^{-2} \left(\frac{\lambda}{\text{mm}} \right)^3, \quad (1)$$

where

$$\kappa_\nu = 0.1 \left(\frac{\nu}{1 \text{ THz}} \right)^\beta \quad (2)$$

The symbols of λ , T , κ_ν , F_ν^{beam} , and θ_{HPBW} in Equation (1) are the wavelength, temperature, dust opacity, flux of dust continuum emission, and half power beam width, respectively. The continuum data wavelength is approximately

Table 2. Identification of cores

Position	R.A. (J2000)	Decl. (J2000)	$\theta_{\text{major}} \times \theta_{\text{minor}}$	Position Angle	V_{sys} (km s $^{-1}$) ^a	Flux (mJy beam $^{-1}$) ^b	N_{H_2} (cm $^{-2}$) ^c
Core A	16 ^h 59 ^m 41 ^s .627	-40°03′43″.61	0′.30 × 0′.25	66°	-17.1	119.0 ± 1.6	5.0 ^{+5.5} _{-2.6} × 10 ²⁴
Core B	16 ^h 59 ^m 41 ^s .586	-40°03′42″.96	0′.70 × 0′.48	108°	-14.6	7.8 ± 1.6	1.9 ^{+2.1} _{-1.0} × 10 ²³
Core C	16 ^h 59 ^m 41 ^s .089	-40°03′39″.03	0′.54 × 0′.47	27°	-11.8	19.2 ± 1.6	4.8 ^{+5.3} _{-2.4} × 10 ²³

NOTE—Core A is identified based on the moment zero map of the H30 α line by the 2D Gaussian fitting. Core B and Core C are identified by the 2D Gaussian fitting of the moment zero image of the CH₃OH ($4_{-2,3} - 3_{-1,2} E$) line.

^aObtained by the Gaussian fitting of the $J = 12 - 11$, $K = 4$ line of CH₃CN.

^bContinuum fluxes with beam sizes of 0′.3 for Core A and 0′.5 for the others, respectively.

^cErrors were derived by changes in assumed temperatures between 50 and 200 K.

1.37 mm. The flux values at each core are summarized in Table 2. These fluxes are beam-averaged values with beam sizes of 0′.3 for Core A and 0′.5 for the others, respectively. We corrected the continuum emission toward Core A by subtracting the free-free continuum emission as we describe in Appendix A. We subtracted this free-free component from the continuum flux and derived the dust continuum emission. H30 α emission toward Core B and Core C was not detected. The dust opacity at the 1.37 mm (κ_{ν}) is calculated using Equation (2) (Planck Collaboration et al. 2011) with $\beta = 1.6$ (Sadavoy et al. 2013). The dust temperature (T) is assumed to be 100 K, because COMs have been detected toward all of the cores as shown in Section 3.2. If we change the temperature between 50 and 200 K, the derived N_{H_2} values change by a factor of ~ 2 . The derived N_{H_2} values are summarized in Table 2.

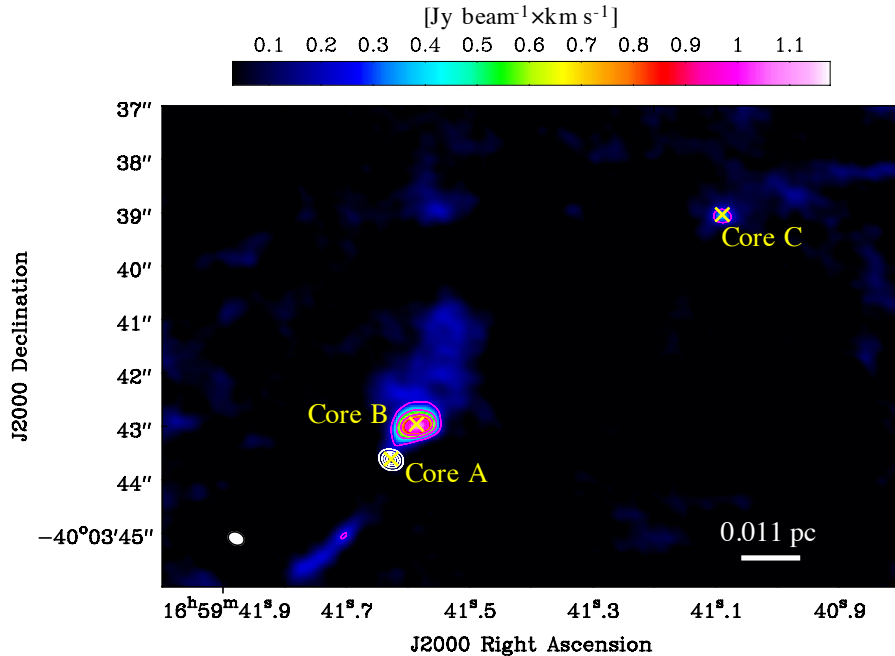


Figure 2. Methanol ($4_{-2,3} - 3_{-1,2} E$) moment zero image (color image and magenta contours) overlaid by the H30 α moment zero image (white contours). The contour levels are 20, 40, 60, and 80% of their peak intensities, which are 1.11 and 11.1 Jy beam $^{-1} \times \text{km s}^{-1}$ for the CH₃OH and H30 α lines, respectively. Yellow crosses indicate the positions of Core A, Core B, and Core C. The white ellipse at the left bottom indicates the angular resolution of approximately 0′.32×0′.25.

3.2. Moment Zero Images

We made moment zero images of each molecular line integrating the whole velocity range where emission is detected. Figure 3 shows the spatial distributions of (a) C¹⁸O (2 – 1), (b) H₂CO (3_{2,2} – 2_{2,1}), (c) DCN (3 – 2), and (d) ³³SO (6₅ – 5₄). Their spatial distributions, except for ³³SO, are relatively extended compared to those of COMs (Figures 4 and 5). The red crosses indicate positions of Cores A to C (Figure 2 and Table 2). Table 3 summarizes species, transition, rest frequency, excitation energy, and peak intensity of each moment zero image analyzed in this work.

The spatial distributions of C¹⁸O and H₂CO show arc-like structures with strong peaks at Core B. There is also weaker emission associated with Core C. In Section 4.2, we discuss the formation mechanisms of H₂CO by comparing between the spatial distributions of C¹⁸O and H₂CO.

The DCN spatial distribution (panel (c) of Figure 3) is different from the above two species. A strong peak is located at Core B and a filamentary structure can be seen at the northern east region, corresponding to the northeast outflow cavity wall (NEC-wall) in Guzmán et al. (2018). Other emission regions are located nearby and to the west of Core C.

Panel (d) of Figure 3 shows a close-up moment zero image of ³³SO (6₅ – 5₄) emission at G345.5+1.47. One ³³SO peak is associated with Core B, and other peaks are located near Core A. The ³³SO emission seems to surround Core A. We discuss the ³³SO spatial distribution around Core A in detail in Section 4.3.

Figures 4 and 5 show moment zero maps of various molecular emission lines more compact morphology. The information of lines and peak intensities for each panel is listed in Table 3. Most of the molecular emissions are associated with both Cores B and C as shown in Figures 4 and 5.

Figure 4 shows the spatial distributions of COMs in panels (a) – (e) and H30 α in panel (f). The CH₃OH (4_{-2,3} – 3_{-1,2} E) line in panel (a) shows more extended spatial distribution than the CH₃OH (20_{-1,19} – 20_{-0,20} E) line in panel (b). This is caused by their different upper energy levels; $E_u/k = 44.5$ K for panel (a) and 508.4 K for panel (b), respectively (Table 3).

The CH₃CN (12 – 11, $K = 3$) line comes from Cores A, B, and C, while the lines of oxygen-bearing COMs mainly come from Core B and Core C (Figure 4). The upper energy level of the CH₃CN line of panel (c) is 133.2 K, which is an intermediate value compared to those of panels (a) and (b). Therefore, the different spatial distributions between CH₃OH and CH₃CN are not brought by the different upper energy level of the lines. The different morphologies between the CH₃OH (4_{-2,3} – 3_{-1,2} E) and the CH₃CN line seem to reflect different origins. As indicated in Figure 6, the CH₃OH (4_{-2,3} – 3_{-1,2} E) line has been detected at Core A, although there is no its emission peak at Core A (panel (a) of Figure 4). Since low excitation energy lines of CH₃OH trace shock regions (e.g., Taniguchi et al. 2020), the CH₃OH line around Core A is possibly originated in a shock region. Shock regions are induced by several star formation phenomena, such as jets and molecular outflows. Guzmán et al. (2011) identified the SE-NW molecular outflow and the central knot of the jet/outflow system is consistent with the Core A position (Guzmán et al. 2010). Alternatively, the CH₃OH line may trace a remnant gas scattered by the HCH II region. The CH₃CN emission, on the other hand, does peak at Core A, which implies thermal sublimation from dust grains.

The spatial distribution of the CH₃OCH₃ (22_{4,19} – 22_{3,20}) lines in panel (d) is similar to that of (CH₃)₂CO (20 – 19) lines in panel (e). The upper energy levels of the lines in panels (d) and (e) are 253.4 K and 119.1 K, respectively (Table 3). Both of these lines likely trace hot core regions. In addition, their distributions at Core B are more compact than that of the CH₃OH (4_{-2,3} – 3_{-1,2} E; $E_u/k = 44.5$ K) line in panel (a), and similar to the CH₃OH (20_{-1,19} – 20_{-0,20} E; $E_u/k = 508.4$ K) line in panel (b). These different spatial distributions seem to reflect lower abundances of CH₃OCH₃ and (CH₃)₂CO compared to the CH₃OH abundance (Section 3.4) and different upper energy levels.

Figure 5 shows the spatial distributions of HC₃N and its ¹³C isotopologues (24 – 23) in panels (a) – (d), ¹³CN (2 – 1) in panel (e), DCN (3 – 2) in panel (f), and HNC (10 – 9) in panels (g) and (h). The vibrationally excited lines of HC₃N ($v_7 = 2$, $J = 24 - 23$) mainly come from Core B, while the ground vibrational state lines ($v = 0$, $J = 24 - 23$) of the ¹³C isotopologues associate with Cores A, B, and C, as shown in panels (a) – (d). The two ¹³C isotopologues of HC₃N, HC¹³CCN and HCC¹³CN, show the same spatial distributions in panels (c) and (d). The more extended distributions of the ¹³C isotopologues are caused by the lower energy levels of the observed lines. In fact, these vibrationally excited lines have extremely high upper energy levels of ~ 775 K, compared to those of the ground vibrational state lines (130.4 K) in panels (c) and (d). The HC₃N spatial distributions are similar to that of CH₃CN (12 – 11), a typical hot core tracer.

The ¹³CN (2 – 1) emission in panel (e) is associated with Core B and its weak emission comes from Core C, while the DCN (3 – 2) distribution in panel (f) shows a more extended structure. The upper energy levels are 15.6 K and

Table 3. Summary of moment zero images

Panel	Species	Transition	Rest Frequency (GHz)	E_u/k (K)	Peak intensity (Jy beam ⁻¹ × km s ⁻¹)
Figure 3					
(a)	C ¹⁸ O	$J = 2 - 1$	219.5603541	15.8	0.60
(b)	H ₂ CO	$J_{Ka,Kc} = 3_{2,2} - 2_{2,1}$	218.475632	68.1	0.74
(c)	DCN	$J = 3 - 2$	217.2385378	20.9	0.33
(d) ^a	³³ SO	$J_N = 6_5 - 5_4, F = \frac{9}{2} - \frac{7}{2}$	217.8271782	34.7	0.28
		$J_N = 6_5 - 5_4, F = \frac{11}{2} - \frac{9}{2}$	217.8298337	34.7	...
		$J_N = 6_5 - 5_4, F = \frac{13}{2} - \frac{11}{2}$	217.8317691	34.7	...
		$J_N = 6_5 - 5_4, F = \frac{15}{2} - \frac{13}{2}$	217.8326422	34.7	...
Figure 4					
(a)	CH ₃ OH	$4_{-2,3} - 3_{-1,2} E$	218.440063	45.5	1.11
(b)	CH ₃ OH	$20_{-1,19} - 20_{-0,20} E$	217.886504	508.4	0.40
(c) ^b	CH ₃ CN	$J = 12 - 11, K = 3$	220.7090165	133.2	1.60
(d) ^a	CH ₃ OCH ₃	$22_{4,19} - 22_{3,20} EA$	217.189668	253.4	0.15
		$22_{4,19} - 22_{3,20} AE$	217.189669	253.4	...
		$22_{4,19} - 22_{3,20} EE$	217.191400	253.4	...
		$22_{4,19} - 22_{3,20} AA$	217.193132	253.4	...
(e) ^{a, b}	(CH ₃) ₂ CO	$20_{2,18} - 19_{3,17} EE$	218.1272074	119.1	0.13
		$20_{3,18} - 19_{3,17} EE$	218.1272074	119.1	...
		$20_{2,18} - 19_{2,17} EE$	218.1272074	119.1	...
		$20_{3,18} - 19_{2,17} EE$	218.1272074	119.1	...
(f)	H30α	...	231.900928	...	11.1
Figure 5					
(a)	HC ₃ N	$v_7 = 2, J = 24 - 23, l = 0$	219.6751141	773.5	0.082
(b)	HC ₃ N	$v_7 = 2, J = 24 - 23, l = 2e$	219.7073487	776.8	0.095
(c)	HC ¹³ CCN	$v = 0, J = 24 - 23$	217.3985682	130.4	0.15
(d)	HCC ¹³ CN	$v = 0, J = 24 - 23$	217.4195740	130.4	0.11
(e) ^a	¹³ CN	$N = 2 - 1, J = \frac{3}{2} - \frac{1}{2}, F_1 = 2 - 1, F = 1 - 0$	217.296605	15.6	0.51
		$N = 2 - 1, J = \frac{5}{2} - \frac{3}{2}, F_1 = 2 - 2, F = 2 - 2$	217.298937	15.7	...
		$N = 2 - 1, J = \frac{3}{2} - \frac{1}{2}, F_1 = 2 - 1, F = 2 - 1$	217.301175	15.6	...
		$N = 2 - 1, J = \frac{3}{2} - \frac{1}{2}, F_1 = 2 - 1, F = 3 - 2$	217.303191	15.6	...
(f)	DCN	$J = 3 - 2$	217.2385378	20.9	0.33
(g) ^a	HNCO	$10_{3,8} - 9_{3,7}$	219.6567695	433.0	0.14
		$10_{3,7} - 9_{3,6}$	219.6567708	433.0	...
(h) ^a	HNCO	$10_{2,9} - 9_{2,8}$	219.7338500	228.3	0.56
		$10_{2,8} - 9_{2,7}$	219.7371930	228.3	...

NOTE—Rest frequency and excitation energy are taken from the Cologne Database for Molecular Spectroscopy (CDMS; Müller et al. 2005).

^aThese lines were not resolved and detected as one line.

^bRest frequency and excitation energy are taken from the Jet Propulsion Laboratory catalog (JPL catalog; Pickett et al. 1998).

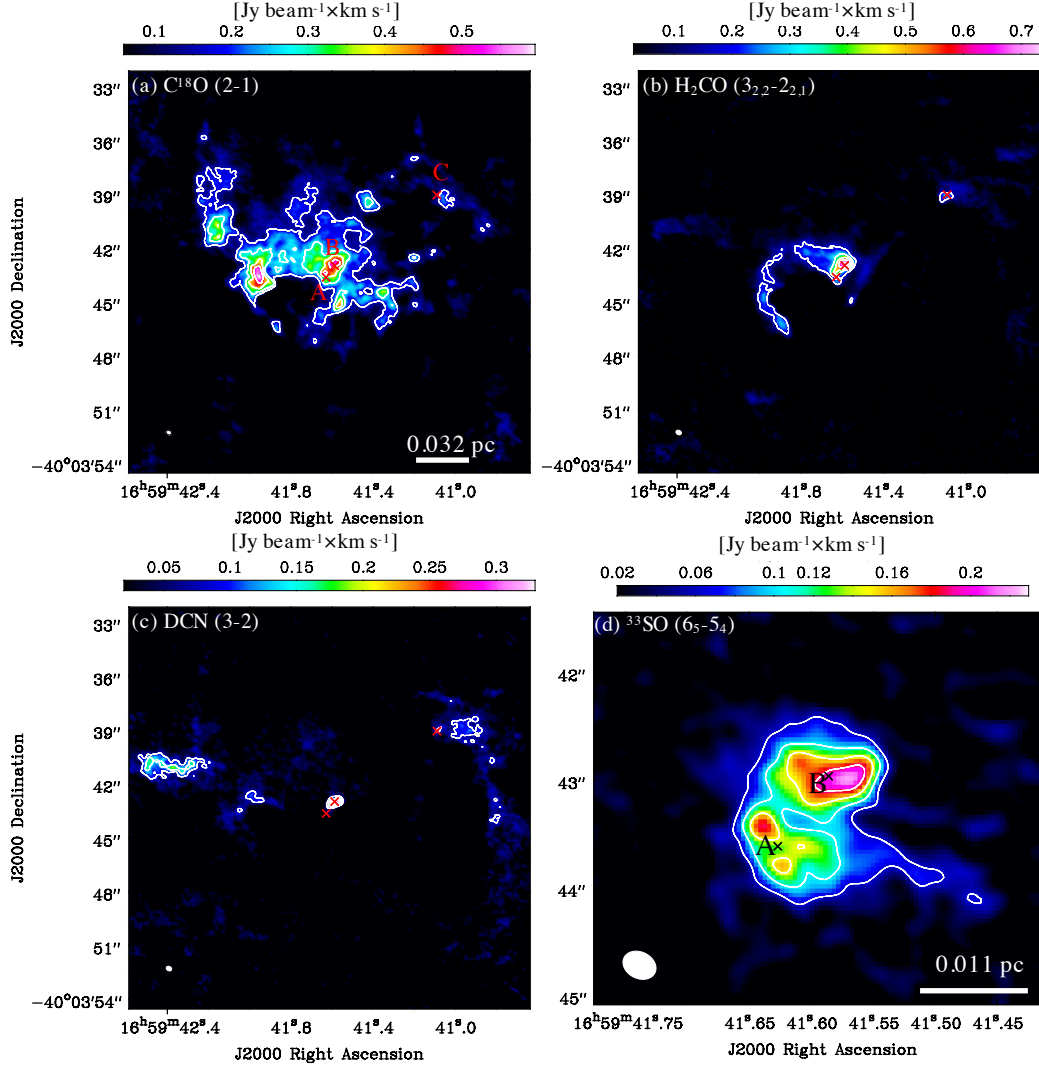


Figure 3. Moment zero images of (a) C^{18}O (2 – 1), (b) H_2CO ($3_{2,2} - 2_{2,1}$), (c) DCN (3 – 2), and (d) ^{33}SO ($6_5 - 5_4$). The contour levels are 20, 40, 60, and 80% of their peak intensities (0.60, 0.74, 0.33, and 0.28 $\text{Jy beam}^{-1} \times \text{km s}^{-1}$ for panels (a) – (d), respectively). The white ellipse at the left bottom indicates the angular resolution of approximately $0''.32 \times 0''.25$. Red crosses in panels (a) – (c) indicate positions of Cores A, B, and C. In panel (d), black crosses show positions of Core A and Core B. The color scales are adjusted from rms noise levels to the peak intensities for each panel.

20.9 K for the ^{13}CN and DCN lines, respectively. Because these are quite similar to each other, different upper energy transition levels is not the main cause of the different spatial distributions of these two species. This difference is more likely to be caused by the different environments traced by each species. The CN/HCN ratio is enhanced in high ultraviolet (UV) flux regions, because HCN is destroyed by the UV radiation forming CN (e.g., Riaz et al. 2018). A possible explanation for the non-detection of the ^{13}CN line at Core A, at which the UV flux is likely strongest in this region, is the selective photodissociation. In order to investigate the effect of the selective photodissociation, we need to observe the H^{13}CN lines and lines of normal species of CN and HCN .

Four HNCO ($10 - 9$) lines also show similar spatial distributions to CH_3CN and HC_3N ; the HNCO lines associate with Cores A, B, and C as shown in panels (g) and (h). The differences in spatial distribution between panels (g) and (h) arises from the different upper energy levels. The upper energy levels of lines in panel (g) are 433.0 K and higher than those in panel (h) (228.3 K), and therefore, the spatial distribution of panel (h) is more extended.

The critical density is another important factor to determine spatial distributions of each line. Since we could not derive accurate densities at each position, we do not discuss the critical density. However, we note that most molecular lines have been detected at Core B, at which the derived H_2 column density is lower than the other cores. This suggests

the upper energy level of the transition is more relevant than the critical density to explain the emission and make the compositions presented in this study.

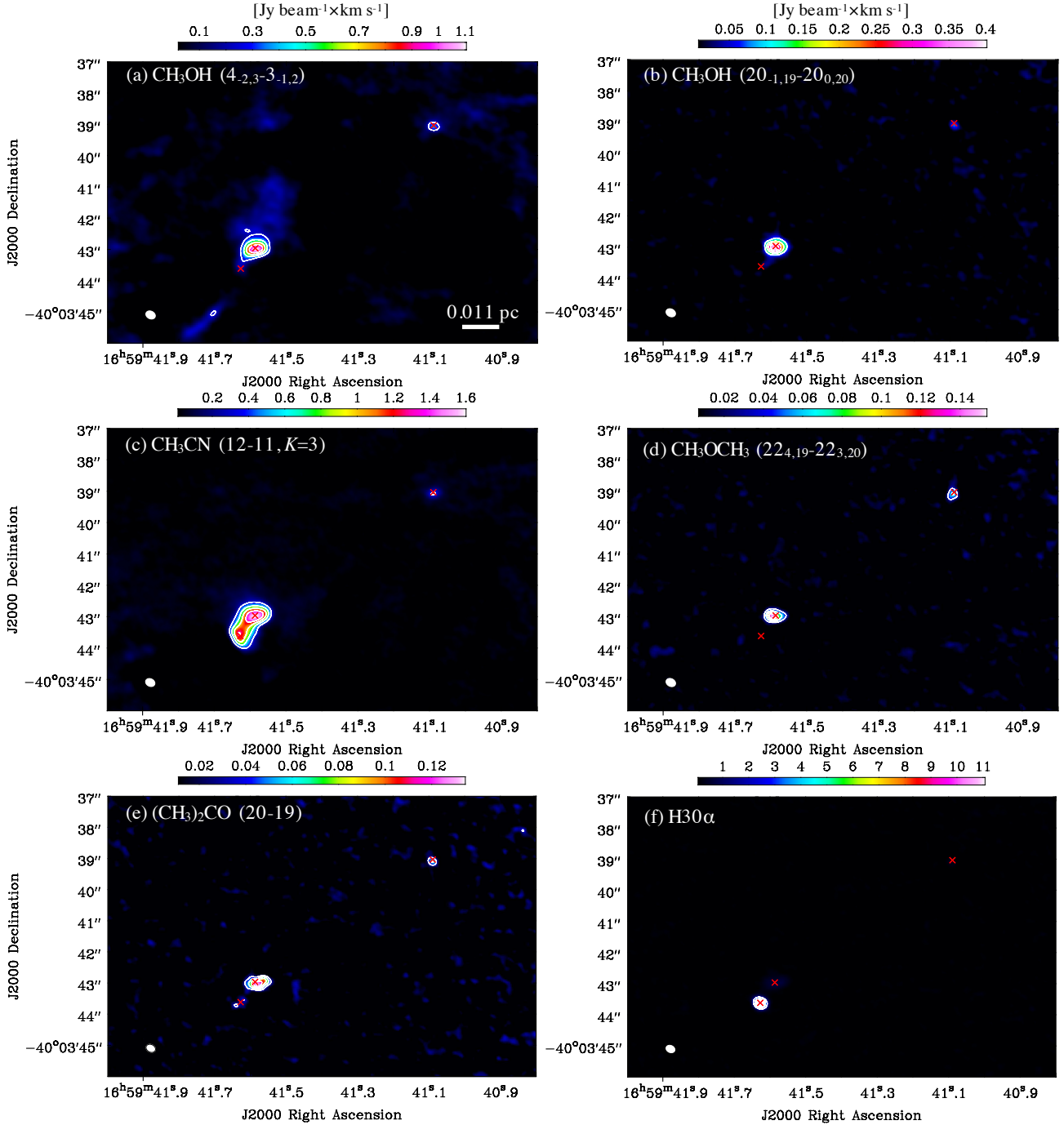


Figure 4. Moment zero images. The contour levels are 20, 40, 60, and 80% of their peak intensities. The full transitions and peak intensities of each panel are summarized in Table 3. The white ellipse at the left bottom indicates the angular resolution of approximately $0''.32 \times 0''.25$. Red crosses indicate positions of Cores A, B, and C. The color scales are adjusted from rms noise levels to the peak intensities for each panel.

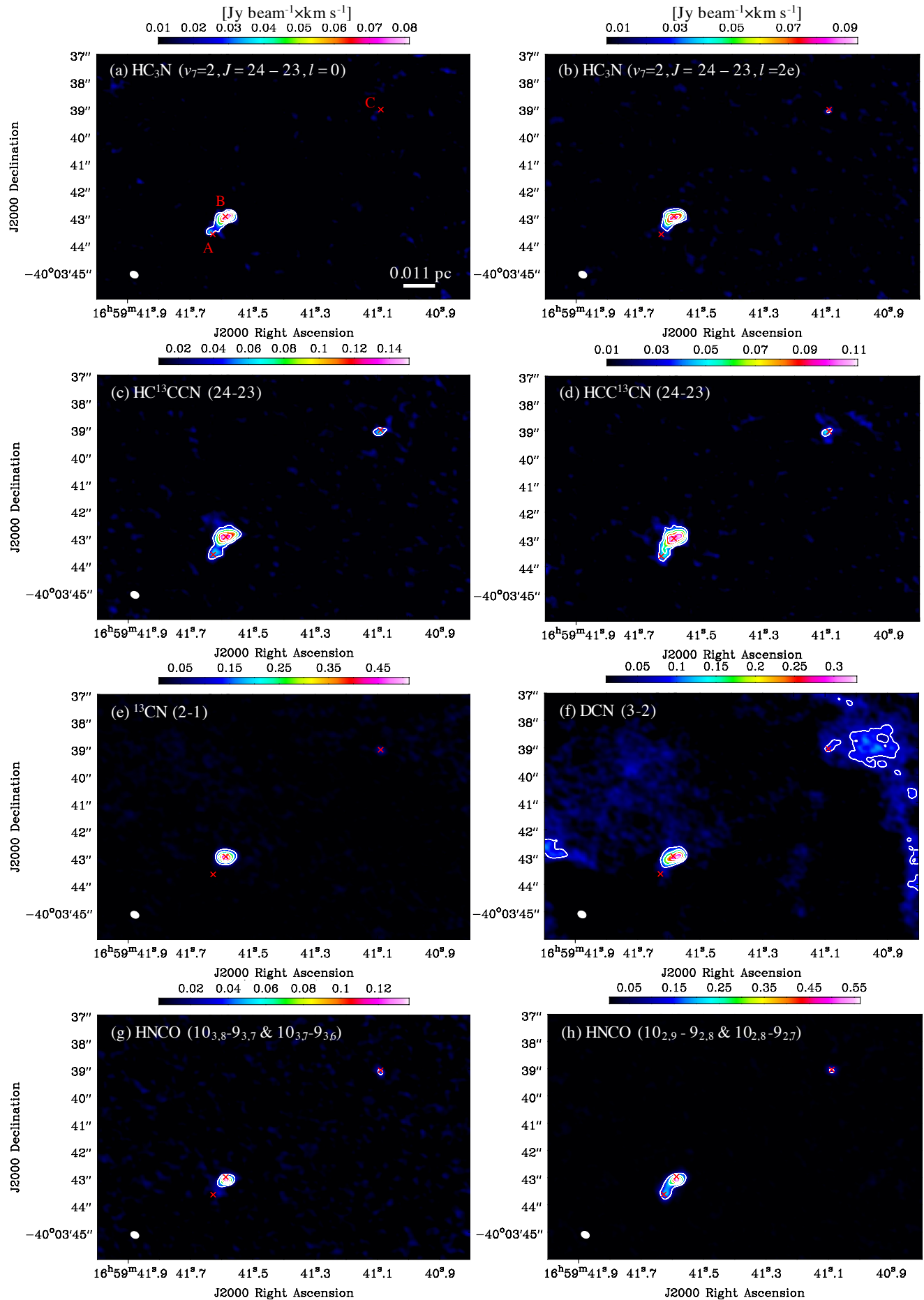


Figure 5. Moment zero images. The contour levels are 20, 40, 60, and 80% of their peak intensities. The transitions and peak intensities of each panel are summarized in Table 3. The white ellipse at the left bottom indicates the angular resolution of approximately $0'32 \times 0'25$. Red crosses indicate positions of Cores A, B, and C. The color scales are adjusted from rms noise levels to the peak intensities for each panel.

3.3. Spectra toward the three cores

Figures 6 and 7 show spectra of the 217.0 – 218.6 GHz and 219.56 – 219.76 GHz bands toward Cores A, B, and C, respectively. Bottom three panels are a zoom of the top three. We identified lines using the CASSIS software with the Cologne Database for Molecular Spectroscopy (CDMS; Müller et al. 2005) and the Jet Propulsion Laboratory catalog (JPL catalog; Pickett et al. 1998). Since the velocity resolution of the final spectra of Figure 6 is low (3 km s^{-1}), some lines could not be identified without ambiguity. At the position of Core C, the ^{33}SO line is detected as a spurious-like line (Figure 6). Such a spurious-like feature is considered to be brought by very low-velocity resolution (3 km s^{-1}). We confirm that it does not affect for other regions. We then neglect the position of Core C in its moment zero image. We did not apply Gaussian fitting for detected lines due to the low velocity resolution. Table 4 summarizes species, transition, rest frequency, and excitation energy of detected lines at each core position.

Core B is the most line-rich position, where various oxygen-bearing COMs, e.g., CH_3OCH_3 and CH_3OCHO , have been detected. Furthermore, vibrational-excited lines of HC_3N , whose upper energy levels are extremely high ($E_u/k \approx 775 \text{ K}$), have been detected.

As shown later, the excitation temperature of CH_3CN is derived to be above 200 K at Core C. Furthermore, the abundances of COMs are high. For example, the CH_3OH abundance is around 10^{-6} (Figure 9). This abundance can be reproduced only after the temperature reaches above 200 K (Taniguchi et al. 2019). These results suggest active hot core chemistry at Core C. Guzmán et al. (2018) also concluded that Core C is associated with a second hot molecular core within IRAS16562–3959, linked to an MYSO less massive than G345.5+1.47. In summary, all of these results imply that a very young star is embedded at Core C.

3.4. Analyses

We analyzed spectra at the three cores using the CASSIS software (Caux et al. 2011). In the analyses presented here, we have used the local thermodynamic equilibrium (LTE) model available in CASSIS spectrum analyzer by assuming lines are optically thin. The rotational diagram fittings of CH_3CN do not show any systematic shifts as shown in Figure 8. Thus, the assumption of optically thin regime seems to be reasonable in our case.

Except for CH_3CN , only one or a few lines with similar excitation energies have been detected for each species. We then applied the Markov Chain Monte Carlo (MCMC) method, which is an interactive process that goes through all of the parameters with a random walk and heads into the solutions space, and χ^2 minimization gives the final solution.

We derive the excitation temperatures and column densities of CH_3CN using its K -ladder lines of the $J = 12 - 11$ transition. Left panels of Figure 8 show spectra of the eight K -ladder lines of the $J = 12 - 11$ transition ($K = 0 - 7$) toward the three cores. The lines from right to left correspond to from $K = 0$ to $K = 7$. We fitted the spectra with a Gaussian profile. We cannot fit the $K = 7$ line toward Core A, and we omitted it from the fitting.

Right panels of Figure 8 show the rotational diagram using the Gaussian fitting results of the left panels. The derived column densities and excitation temperatures are summarized in Table 5. The column densities and excitation temperatures are $(1.0 \pm 0.1) \times 10^{16} \text{ cm}^{-2}$ and $279 \pm 57 \text{ K}$, $(1.4 \pm 0.2) \times 10^{16} \text{ cm}^{-2}$ and $420 \pm 117 \text{ K}$, and $(1.3 \pm 0.2) \times 10^{15} \text{ cm}^{-2}$ and $213 \pm 25 \text{ K}$ at Cores A, B, and C, respectively. Although we assumed that the CH_3CN lines are optically thin, we cannot rule out the optically thick case due to the scatter. The plots for the first three K -ladder lines ($K = 0 - 2$) are coincident with each other within their errors, but the plots for the $K = 0$ line may be slightly lower than the other two plots. If the lines are optically thick, the derived rotational temperature should be overestimated (Beltrán et al. 2011; Furuya et al. 2011).

We derived the column densities and excitation temperatures of other species using the MCMC method and the LTE model in the CASSIS software. We considered the following two cases:

1. assume excitation temperatures between 50 and 200 K, and
2. assume a range of temperatures around the excitation temperatures derived by the CH_3CN fitting.

We assume the excitation temperature range of the first case taking the typical temperature at the hot core of 100 K into consideration. For the second case, we tested the following temperature ranges: 220 – 340 K for Core A, 250 – 540 K for Core B and 185 – 240 K for Core C, respectively.

We fixed source sizes, or size of the emitting region, to $0''.3$ for Core A and $0''.5$ for Core B and Core C, respectively (Table 2). Because the cores appear to be resolved, we assume a filling factor of unity. The line width (full width half maximum; FWHM) was treated as a free parameter, constrained between 1 and 10 km s^{-1} . The line widths derived

Table 4. Summary of detected lines

Species	Transition	Rest Frequency (GHz)	E_u/k (K)	Core A ^a	Core B ^a	Core C ^a
(CH ₃) ₂ CO	19 _{3,16} – 18 _{4,15} , 19 _{4,16} – 18 _{3,15}	217.0225	115.5	N	Y	(Y)
¹³ CN	$N = 2 - 1, J = 3/2 - 3/2, F_1 = 1 - 1, F = 1 - 2$	217.046988	15.7	N	Y	(Y)
	$N = 2 - 1, J = 3/2 - 3/2, F_1 = 1 - 1, F = 2 - 1$	217.0728010	15.7	N	Y	(Y)
SiO	$v = 0, J = 5 - 4$	217.104980	31.3	Y	(Y)	Y
CH ₃ OCH ₃ ^b	22 _{4,19} – 22 _{3,20} EA	217.189668	253.4	N	Y	Y
	22 _{4,19} – 22 _{3,20} AE	217.189669	253.4	N	Y	Y
	22 _{4,19} – 22 _{3,20} EE	217.191400	253.4	N	Y	Y
	22 _{4,19} – 22 _{3,20} AA	217.193132	253.4	N	Y	Y
DCN	$J = 3 - 2$	217.2385378	20.9	Y	Y	Y
¹³ CN	$N = 2 - 1, J = 3/2 - 1/2, F_1 = 1 - 0, F = 0 - 1$	217.264639	15.7	N	Y	N
	$N = 2 - 1, J = 5/2 - 3/2$	217.296605	15.7	N	Y	Y
	$N = 2 - 1, J = 5/2 - 3/2, F_1 = 2 - 2, F = 2 - 3$	217.315147	15.7	N	Y	N
HC ¹³ CCN	$J = 24 - 23$	217.3985682	130.4	Y	Y	Y
HCC ¹³ CN	$J = 24 - 23$	217.419574	130.4	Y	Y	Y
¹³ CN	$N = 2 - 1, J = 5/2 - 3/2, F_1 = 2 - 1, F = 3 - 2$	217.4285632	15.7	N	Y	(Y)
(CH ₃) ₂ CO	18 _{12,6} – 17 _{13,4}	217.5921139	141.3	N	N	(Y)
	23 _{20,3} – 22 _{21,1} ^b	217.6552	248.3	N	Y	(Y)
	37 _{12,25} – 37 _{11,26} , 37 _{13,25} – 37 _{12,26} ^b	217.6553	493.2	N	Y	(Y)
³³ SO ^b	$J_N = 6_5 - 5_4, F = \frac{9}{2} - \frac{7}{2}$	217.8271782	34.7	Y	Y	(Y)
	$J_N = 6_5 - 5_4, F = \frac{11}{2} - \frac{9}{2}$	217.8298337	34.7	Y	Y	(Y)
	$J_N = 6_5 - 5_4, F = \frac{13}{2} - \frac{11}{2}$	217.8317691	34.7	Y	Y	(Y)
	$J_N = 6_5 - 5_4, F = \frac{15}{2} - \frac{13}{2}$	217.8326422	34.7	Y	Y	(Y)
CH ₃ OH	20 _{-1,19} – 20 _{-0,20} E	217.886504	508.4	N	Y	Y
(CH ₃) ₂ CO	20 _{2,18} – 19 _{3,17} , 20 _{3,18} – 19 _{2,17}	218.0914	119.2	N	Y	(Y)
	32 _{22,10} – 32 _{19,13}	218.1059	438.9	N	Y	(Y)
	20 _{2,18} – 19 _{3,17} , 20 _{3,18} – 19 _{3,17} , 20 _{2,18} – 19 _{2,17}	218.1272	119.1	N	Y	(Y)
	20 _{2,18} – 19 _{3,17} , 20 _{3,18} – 19 _{2,17}	218.1629	119.0	N	Y	(Y)
H ₂ CO	3 _{0,3} – 2 _{0,2}	218.2222	21.0	Y	Y	Y
CH ₃ OCHO	17 _{3,14} – 16 _{3,13}	218.2809	99.7	N	Y	Y
	17 _{3,14} – 16 _{3,13}	218.2979	99.7	N	Y	Y
HC ₃ N	$v = 0, J = 24 - 23$	218.3247	131.0	Y	Y	Y
CH ₃ OH	4 _{-2,3} – 3 _{-1,2}	218.440063	45.5	Y	Y	Y
H ₂ CO	3 _{2,2} – 2 _{2,1}	218.4756	68.1	Y	Y	Y
CH ₃ OCH ₃	23 _{3,21} – 23 _{2,22}	218.4898	263.8	N	Y	(Y)
	23 _{3,21} – 23 _{2,22}	218.4924	263.8	N	Y	(Y)
	23 _{3,21} – 23 _{2,22}	218.495	263.8	N	Y	(Y)
(CH ₃) ₂ CO	19 _{12,8} – 18 _{13,5}	218.5439	154.3	N	Y	(Y)
C ¹⁸ O	$J = 2 - 1$	219.5603541	15.8	Y	Y	Y
HNCO ^b	10 _{3,8} – 9 _{3,7}	219.6567695	433.0	N	Y	N
	10 _{3,7} – 9 _{3,6}	219.6567708	433.0	N	Y	N
HC ₃ N	$v_7 = 2, J = 24 - 23, l = 0$	219.67465	769.7	N	Y	N
	$v_7 = 2, J = 24 - 23, l = 2e$	219.70689	772.3	N	Y	N
HNCO	10 _{2,9} – 9 _{2,8}	219.7338500	228.3	Y	Y	(Y)
	10 _{2,8} – 9 _{2,7}	219.7371930	228.3	Y	Y	(Y)
HC ₃ N	$v_7 = 2, J = 24 - 23, l = 2f$	219.74174	772.3	N	Y	N

NOTE—Rest frequency and excitation energy are taken from the Cologne Database for Molecular Spectroscopy (CDMS; Müller et al. 2005) and the Jet Propulsion Laboratory catalog (JPL catalog; Pickett et al. 1998).

^a“Y” and “N” mean detection and non-detection at each core, respectively. The symbol of (Y) means tentative detection.

^bThese lines were not resolved and detected as one line.

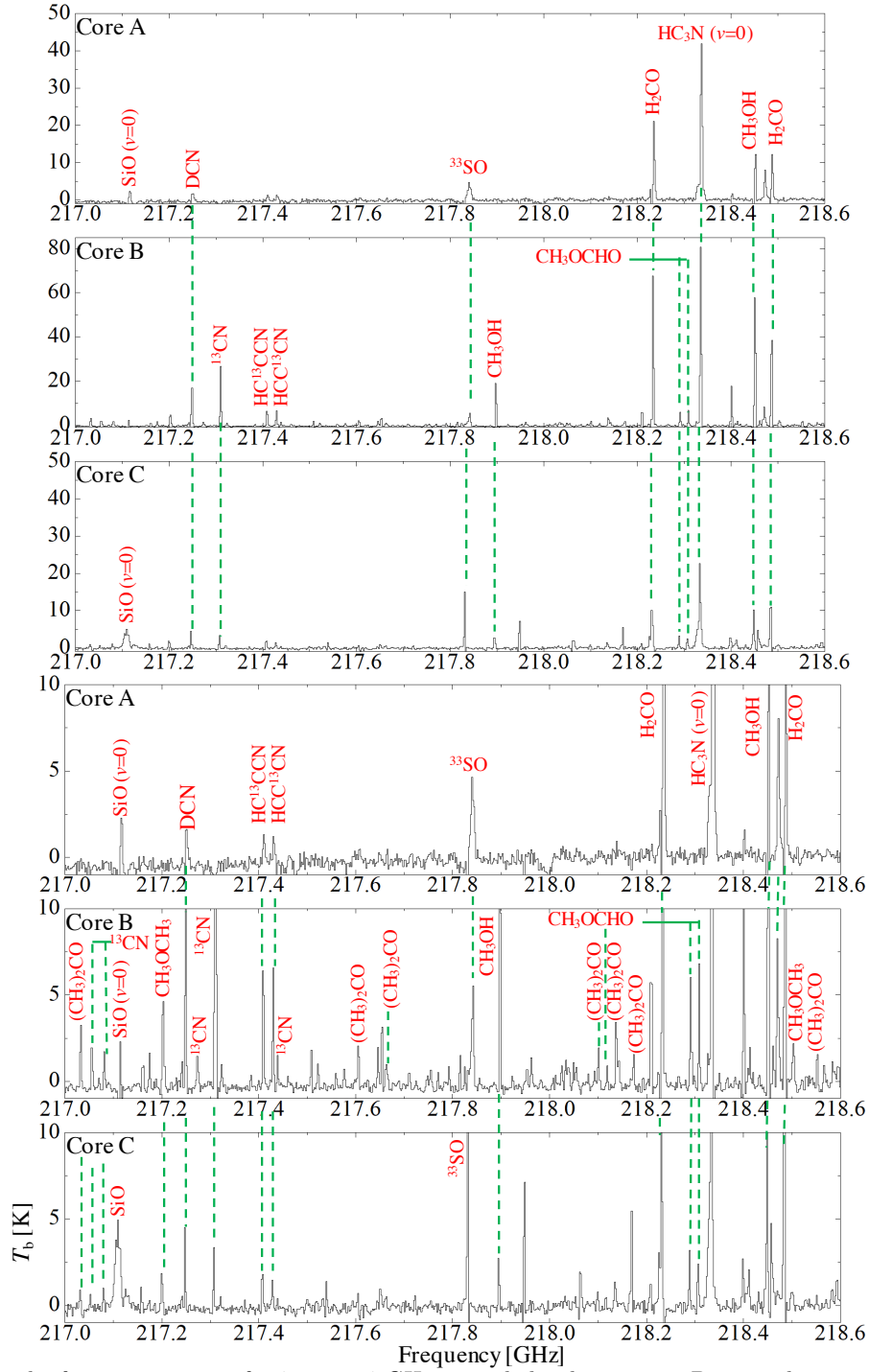


Figure 6. Spectra in the frequency range of 217.0–218.4 GHz toward the three cores. Bottom three panels are a zoom of the top three.

by the fitting are $\sim 2 - 4 \text{ km s}^{-1}$ for Core A and Core B, and $\sim 3 - 5 \text{ km s}^{-1}$ for Core C, respectively. Derived line widths agree well with those of typical hot cores.

Table 6 summarizes the derived column densities and excitation temperatures of the detected species except for CH_3CN toward each core. The “Case 1” and “Case 2” represent the different assumed excitation temperature ranges, as described above. The excitation temperatures of H_2CO and CH_3OH are consistent within their standard deviation errors in all of cases. Other oxygen-bearing COMs (CH_3OCHO , CH_3OCH_3 , and $(\text{CH}_3)_2\text{CO}$) have similar excitation

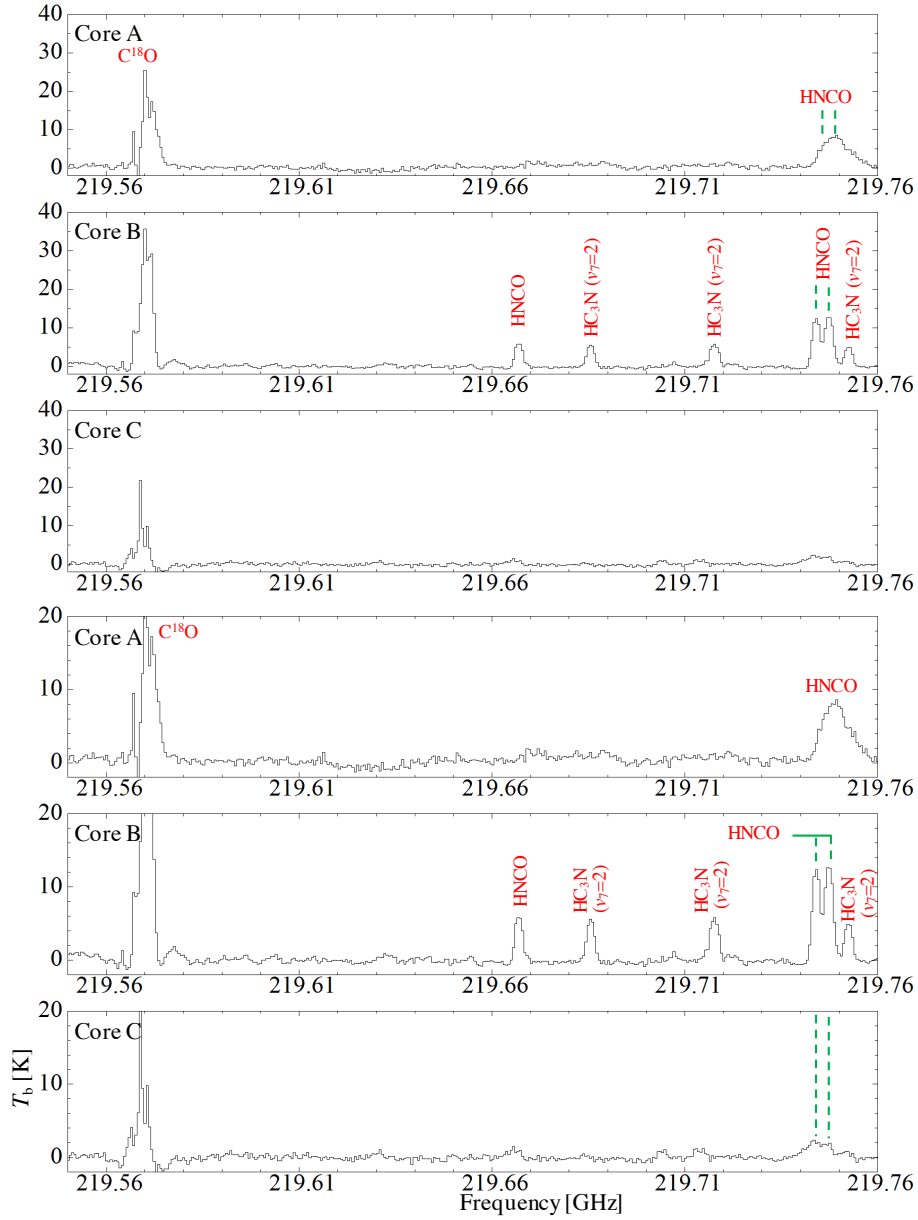


Figure 7. Spectra in the frequency range of 219.55–219.76 GHz toward the three cores. Bottom three panels are a zoom of the top three.

Table 5. Column density and excitation temperature of CH_3CN at the three cores

Position	N (cm^{-2})	T_{ex} (K)
Core A	$(1.0 \pm 0.1) \times 10^{16}$	279 ± 57
Core B	$(1.4 \pm 0.2) \times 10^{16}$	420 ± 117
Core C	$(1.3 \pm 0.2) \times 10^{15}$	213 ± 25

NOTE—Errors represent the standard deviation.

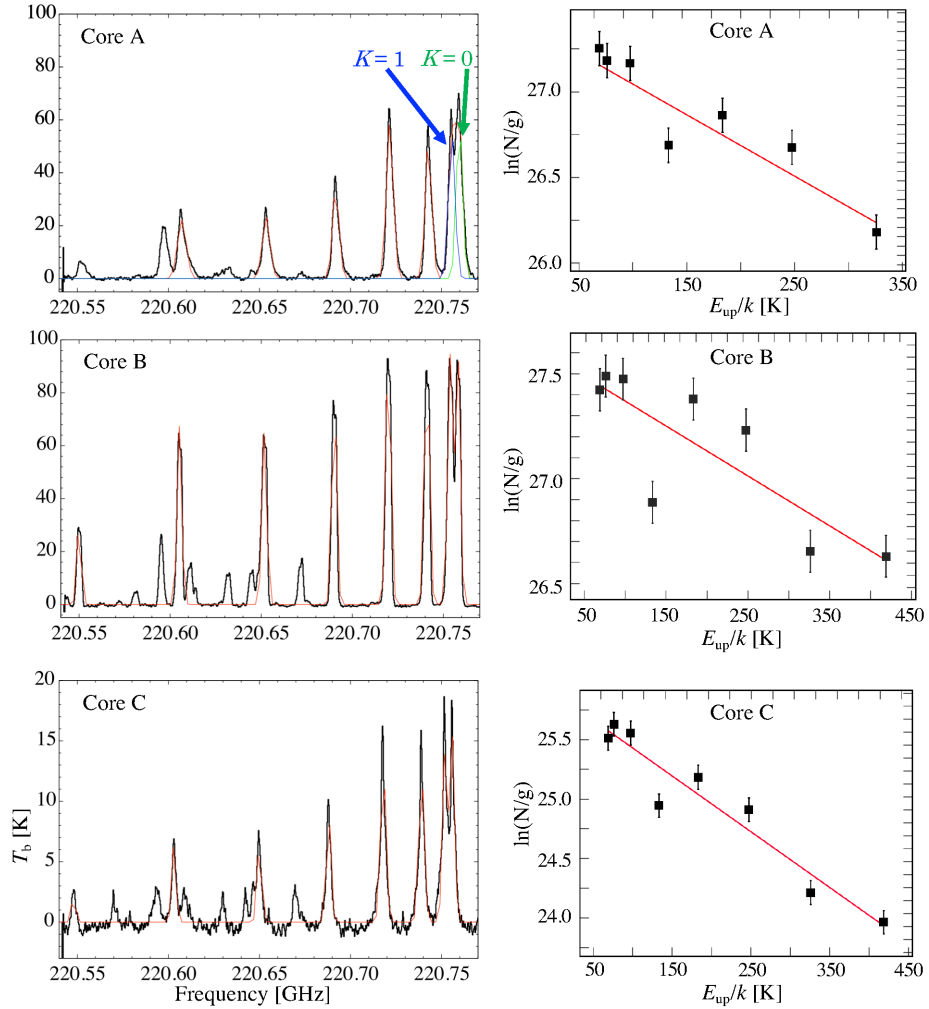


Figure 8. Left panels; spectra of the $J = 12 - 11$ transition lines of CH_3CN toward Cores A, B, and C. Red lines indicate the results of the Gaussian fitting. Right panels; rotational diagrams toward Cores A, B, and C. Red lines show the fitting results, synthesized spectra of the Gaussian fitting for each line. At Core A, green and blue lines indicate the Gaussian fitting for the $K = 0$ and $K = 1$ lines.

temperatures, except for $(\text{CH}_3)_2\text{CO}$ assuming Case 1 toward Core C. Although there is a large uncertainty of the CH_3CN excitation temperature at Core B, the excitation temperatures of all the species are coincident with each other at each core in Case 2. We will discuss comparisons of the chemical compositions between Cores B and C in Section 4.1 with the results of Case 2.

4. DISCUSSIONS

4.1. Comparison of the Chemical Composition Between Core B and Core C

We derived fractional abundances, $X(\text{molecules}) = N(\text{molecules})/N_{\text{H}_2}$, of each species toward Cores B and C, and compare them as shown in Figure 9. We took the errors from both $N(\text{molecules})$ and N_{H_2} into consideration.

The observed H_2CO and CH_3OH abundances at Cores B and C can be reproduced after their thermal desorption from dust grains (Figure 13 in Appendix B and Figure 6 of Taniguchi et al. (2019)). The thermal desorption of H_2CO and CH_3OH occurs at ~ 50 K and ~ 100 K, respectively. Abundances of other COMs ($\sim 10^{-8} - 10^{-7}$) are reproduced in a hot core model with temperature above 100 K (Garrod 2013). These results suggest hot core chemistry is taking place at both Core B and Core C.

All of the species have larger fractional abundances at Core B compared to Core C. While the fractional abundances of CH_3OH and H_2CO at Core B are higher than those at Core C by a factor of $\simeq 100$, the differences in fractional abundances of other species are around one order of magnitude. Methanol (CH_3OH) is important for formation of

Table 6. Derived column density and excitation temperature

Species	Core A		Core B		Core C	
	N (cm $^{-2}$)	T_{ex} (K)	N (cm $^{-2}$)	T_{ex} (K)	N (cm $^{-2}$)	T_{ex} (K)
Case 1 ^a						
CH ₃ OH	$(4.3 \pm 2.3) \times 10^{19}$	98 ± 14	$(3.8 \pm 0.6) \times 10^{18}$	169 ± 20	$(4.4 \pm 4.8) \times 10^{18}$	58 ± 4
HC ₃ N	$(1.6 \pm 0.7) \times 10^{17}$	135 ± 50	$(1.1 \pm 0.4) \times 10^{18}$	99 ± 28	$(1.4 \pm 0.8) \times 10^{18}$	60 ± 9
HC ¹³ CCN	$(3.1 \pm 0.7) \times 10^{14}$	130 ± 37	$(6.9 \pm 1.4) \times 10^{14}$	103 ± 30	$(6.1 \pm 1.9) \times 10^{13}$	76 ± 19
HCC ¹³ CN	$(2.4 \pm 0.6) \times 10^{14}$	130 ± 38	$(4.8 \pm 0.9) \times 10^{14}$	111 ± 23	$(1.3 \pm 0.3) \times 10^{14}$	92 ± 32
H ₂ CO	$(1.4 \pm 0.7) \times 10^{17}$	96 ± 37	$(8.0 \pm 6.3) \times 10^{18}$	140 ± 16	$(6.2 \pm 3.4) \times 10^{16}$	59 ± 6
CH ₃ OCHO	$(8.3 \pm 1.4) \times 10^{16}$	60 ± 6	$(3.2 \pm 0.7) \times 10^{16}$	79 ± 18
CH ₃ OCH ₃	$(4.0 \pm 0.5) \times 10^{17}$	64 ± 5	$(2.1 \pm 0.9) \times 10^{17}$	62 ± 11
(CH ₃) ₂ CO	$(8.3 \pm 1.0) \times 10^{15}$	66 ± 8	$(7.2 \pm 2.1) \times 10^{15}$	122 ± 24
HNCO	$(7.0 \pm 3.6) \times 10^{16}$	82 ± 14	$(6.5 \pm 1.1) \times 10^{15}$	134 ± 17
Case 2 ^b						
CH ₃ OH	$(9.6 \pm 8.9) \times 10^{17}$	256 ± 16	$(7.4 \pm 3.4) \times 10^{18}$	300 ± 31	$(3.2 \pm 1.5) \times 10^{17}$	209 ± 11
HC ₃ N	$(9.1 \pm 6.5) \times 10^{17}$	245 ± 14	$(1.2 \pm 0.9) \times 10^{18}$	278 ± 18	$(9.0 \pm 6.3) \times 10^{17}$	193 ± 4
HC ¹³ CCN	$(3.5 \pm 0.5) \times 10^{14}$	280 ± 35	$(8.3 \pm 1.1) \times 10^{14}$	363 ± 57	$(6.8 \pm 4.7) \times 10^{13}$	192 ± 3
HCC ¹³ CN	$(2.7 \pm 0.5) \times 10^{14}$	281 ± 28	$(6.1 \pm 1.0) \times 10^{14}$	349 ± 59	$(1.1 \pm 0.2) \times 10^{14}$	205 ± 14
H ₂ CO	$(1.5 \pm 0.5) \times 10^{17}$	258 ± 30	$(1.9 \pm 1.6) \times 10^{18}$	278 ± 14	$(2.2 \pm 0.4) \times 10^{16}$	204 ± 8
CH ₃ OCHO	$(9.5 \pm 2.2) \times 10^{16}$	277 ± 21	$(6.2 \pm 1.7) \times 10^{16}$	216 ± 12
CH ₃ OCH ₃	$(7.9 \pm 4.0) \times 10^{16}$	272 ± 19	$(3.2 \pm 0.5) \times 10^{16}$	192 ± 5
(CH ₃) ₂ CO	$(7.8 \pm 2.6) \times 10^{16}$	264 ± 15	$(8.9 \pm 0.9) \times 10^{15}$	192 ± 6
HNCO	$(1.4 \pm 0.3) \times 10^{16}$	297 ± 30	$(4.0 \pm 0.3) \times 10^{15}$	196 ± 6

^aAssume that excitation temperatures are between 50 and 200 K.

^bUse the excitation temperatures derived by the CH₃CN fitting.

oxygen-bearing COMs (Öberg et al. 2009). Hence, oxygen-bearing COMs except for H₂CO and CH₃OH are expected to be formed later than H₂CO and CH₃OH. These results suggest that Core B is more chemically rich or a more evolved hot core with enough time for molecules to sublimate from dust grains and newly form in the hot gas.

4.2. Formation Mechanisms of H₂CO

Most of COMs are generally abundant in hot core regions with temperatures above 100 K where ice mantles sublimate. As shown in Figures 3 and 4, the spatial distribution of H₂CO is different from distributions of other oxygen-bearing COMs; the distribution of H₂CO shows an arc-like structure with a strong peak at Core B, while other COMs are concentrated at Core B and Core C. Such different spatial distributions may suggest that the main formation mechanism of H₂CO is different from those of other COMs. In this subsection, we discuss possible main formation mechanisms of H₂CO.

According to Taniguchi et al. (2019), the formation mechanisms of H₂CO are highly sensitive to the physical evolution of the cores. Based on this, we can clearly distinguish three major formation processes of H₂CO (Figure 13 in Appendix B):

1. formation in the gas-phase through the reaction $\text{CH}_3 + \text{O} \rightarrow \text{H}_2\text{CO} + \text{H}$, active in cold starless core phase when $T \approx 10$ K and $n_{\text{H}} \approx 10^4 - 10^7$ cm $^{-3}$;
2. non-thermal desorption of H₂CO ice formed through the successive hydrogenation of CO ice (ice-H + ice-CO \rightarrow ice-HCO, ice-HCO + ice-H \rightarrow ice-H₂CO) active in the lukewarm stage when 10 K $< T < 25$ K and $n_{\text{H}} \approx 10^7$ cm $^{-3}$;
3. thermal-evaporation of H₂CO ice, active in hot-core stage when $T > 50$ K and $n_{\text{H}} \approx 10^7$ cm $^{-3}$.

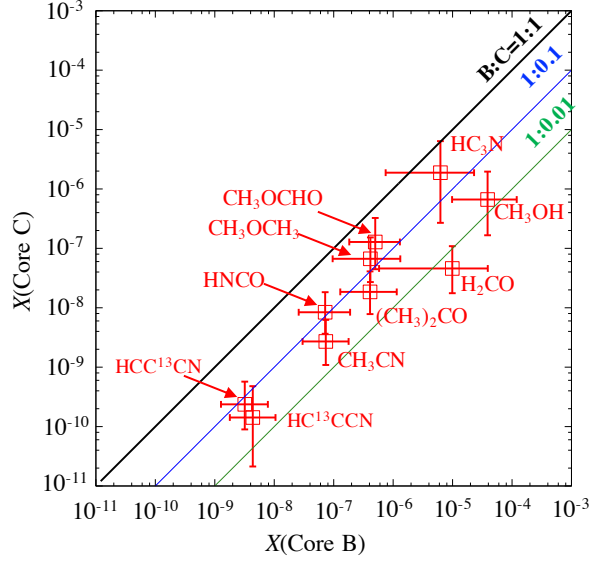


Figure 9. Comparison of chemical compositions between Cores B and C. The black, blue and green lines indicate $X(\text{Core B}) = X(\text{Core C})$, $X(\text{Core B}) = 10 \times X(\text{Core C})$, and $X(\text{Core B}) = 100 \times X(\text{Core C})$, respectively.

Figure 10 shows the spatial distributions of C^{18}O (color) and H_2CO (white contours). Their spatial distributions show a similar structure; an arc-like extended structure and a strong peak at Core B. The extended structure seems to suggest that heating sources are not necessary for formation of the gas-phase H_2CO . This means that either gas-phase formation or non-thermal desorption is important for H_2CO . The similar spatial distributions of C^{18}O and H_2CO support the grain-surface formation and non-thermal desorption. Still, it does not mean that gas-phase formation is irrelevant for H_2CO . To distinguish the two reactions, we need further observations, e.g., O I distribution.

The H_2CO abundance with respect to H_2 at Core B is derived to be around 10^{-5} (Figure 9). This abundance can be reproduced only after thermal evaporation of H_2CO (Figure 13) with temperatures above 50 K. Since many COMs have been detected at Core B, the dust temperature is expected to be above 100 K. Thus, the thermal evaporation seems to work efficiently at this position.

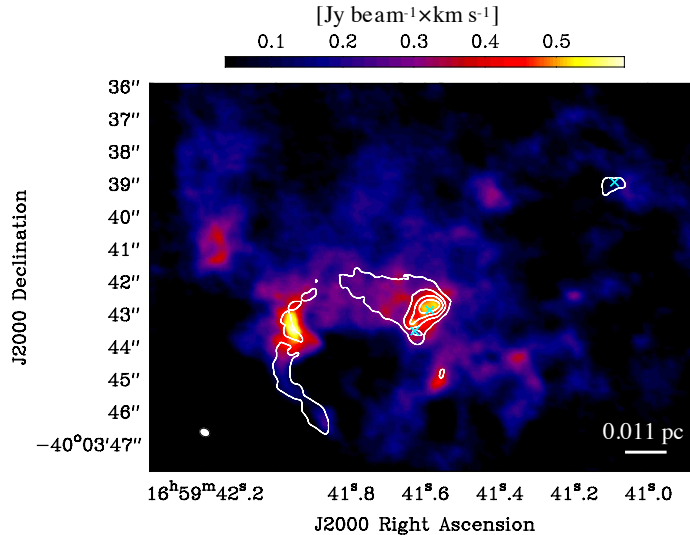


Figure 10. Comparison of spatial distributions of C^{18}O (color) and H_2CO (white contours; the contour levels are 20, 40, 60, and 80% of its peak intensity of $0.74 \text{ Jy beam}^{-1} \times \text{km s}^{-1}$). Cyan crosses indicate positions of Cores A, B, and C.

4.3. Spatial distribution of ^{33}SO emission around Core A

Guzmán et al. (2014) showed the spatial distributions of sulfur-bearing species, SO, SO₂, CS, and OCS, with an angular resolution of $\sim 2''.3 \times 1''.3$. They found that the emission lines of these species come from a molecular core with a size of around 3000 au at the G345.5+1.47 MYSO. Guzmán et al. (2014) suggested that the observed SO emission and morphology at Core B can be understood qualitatively using the predictions of hot gaseous phase chemical models (e.g., van der Tak et al. 2003). Panel (d) of Figure 3 shows a ring-like distribution of ³³SO around Core A. Such a structure has been found for the first time in this source owing to the high spatial resolution. In this subsection, we discuss such this ³³SO structure.

Figure 11 shows the spatial distributions of ³³SO (color) and H30 α (magenta contours) emissions. The strong emission peaks of ³³SO are located at the outer edge of H30 α emission. There are two possible scenarios for such a ring-like structure around the HCH II region; one is molecular destruction by the UV radiation from the central star, and the other is the gas-phase formation of SO at this position. If such a ring-like structure has been formed by molecular destruction by the UV radiation from the central star, other molecules are expected to show similar structures. However, we do not find ring-like structures in moment zero images of other molecules (Figures 4 and 5). This implies that the destruction did not produce the ring-like structure of ³³SO emission by the UV radiation from the central star.

Sulfur monoxide (SO) is considered as a shock tracer. At Core A, shocks can be produced by a molecular outflow and an expanding motion of the HCH II region. However, the morphology of the ³³SO emission does not match the orientation of the molecular outflow nor jet reported by Guzmán et al. (2011). Hence, the molecular outflow does not seem to be an origin of the ³³SO emission feature. In summary, ³³SO is expected to be enhanced in shock regions produced by an interaction between a thick cloud and an expanding motion of the HCH II region. In shock regions, SO is considered to be formed by the following reactions (Esplugues et al. 2014):



and



Esplugues et al. (2014) suggested that the reaction (3) is efficient just after the shock passes and the temperature is still high ($T \geq 1000$ K), while the reaction (4) becomes more efficient in cool gas regions. According to the Kinetic Database for Astrochemistry (KIDA: <http://kida.astrophy.u-bordeaux.fr/>), the α values for the reaction rate coefficients, defined as $k = \alpha(T/300)^\beta \exp(-\gamma/T) \text{ cm}^3 \text{ s}^{-1}$, are 2.1×10^{-12} and 6.6×10^{-11} for reactions (3) and (4), respectively. The γ values for both of the reactions are reported as zero (Vidal et al. 2017). Therefore, the reaction (4) is expected to proceed faster than the reaction (3), and could be a main formation pathway of SO around the observed HCH II region.

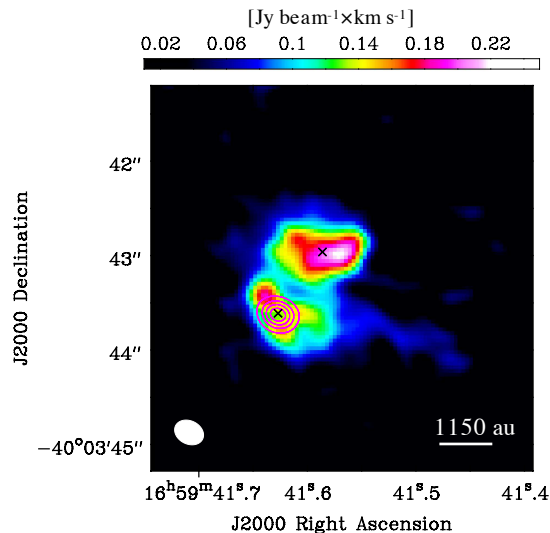


Figure 11. Comparison of spatial distributions of ³³SO (color) and H30 α (magenta contours; the contour levels are 20, 40, 60, and 80% of its peak intensity of $11.1 \text{ Jy beam}^{-1} \times \text{km s}^{-1}$). Black crosses indicate positions of Core A and Core B.

5. CONCLUSION

We have analyzed the ALMA cycle 2 data toward the IRAS 16562–3959 high-mass star-forming region. We spatially resolve the central bright sources into a binary system, a HCH II region and a younger molecule-rich core. We identified molecular emission cores using the moment zero images of the H30 α line and a CH₃OH line, which we name Cores A, B, and C. We have detected several oxygen-bearing COMs, CH₃CN, and HC₃N and derived their column densities and excitation temperatures at three cores. While oxygen-bearing COMs have been detected toward Cores B and C, CH₃CN, HC₃N, and HNCO are located in all of the cores.

We compare the chemical composition between Core B and Core C. The fractional abundances at Core B are higher than those at Core C by around one order of magnitude, while the fractional abundances of CH₃OH and H₂CO at Core B are higher by a factor of $\simeq 100$. These results seem to imply that Core B is a more evolved hot core, where enough time has elapsed for molecules to sublimate from dust grains and new molecules to form in the hot gas.

We investigate the main formation mechanism of H₂CO toward this high-mass star-forming region by a comparison of the spatial distributions between H₂CO and C¹⁸O. Their extended arc-like structure suggests that gas-phase reaction and/or a grain surface reaction followed by non-thermal evaporation are likely formation routes of the gas-phase H₂CO. The enhancement of the gas-phase H₂CO at Core B also indicates efficient thermal evaporation of H₂CO.

The spatial distribution of ³³SO around Core A shows a unique structure distributing at the outer edge of the H30 α emission region. These results seem to indicate that ³³SO is enhanced in a shock region produced by an expanding motion of the HCH II region.

ACKNOWLEDGMENTS

This paper makes use of the following ALMA data: ADS/JAO.ALMA#2013.1.00489.S. ALMA is a partnership of ESO (representing its member states), NSF (USA) and NINS (Japan), together with NRC (Canada), MOST and ASIAA (Taiwan), and KASI (Republic of Korea), in cooperation with the Republic of Chile. The Joint ALMA Observatory is operated by ESO, AUI/NRAO and NAOJ. Based on analysis carried out with the CASSIS software and JPL and CDMS spectroscopic databases. CASSIS has been developed by IRAP-UPS/CNRS (<http://cassis.irap.omp.eu>). This work was supported by JSPS KAKENHI Grant Number JP20K14523.

Facilities: Atacama Large Millimeter/submillimeter Array (ALMA)

Software: Common Astronomy Software Applications package (CASA; McMullin et al. 2007), CASSIS (Caux et al. 2011)

APPENDIX

A. H30 α SPECTRA TOWARD CORE A

Figure 12 shows a spectra of the H30 α line (231.9009 GHz) toward Core A. A Gaussian fitting to the line is shown with a red line in Figure 12. The peak intensity and full width half maximum (FWHM) were derived to be 46.7 ± 0.3 K (1σ) and 49.5 ± 0.3 km s⁻¹, respectively.

Under LTE conditions, the line optical depth of the recombination line is given by $\mathcal{T}_L\phi(\nu)$, where \mathcal{T}_L is defined in Equation (B5) in Guzmán et al. (2014) and $\phi(\nu)$ is the line profile. Dividing \mathcal{T}_L by the free-free opacity τ_{ff} (e.g. Wilson et al. 2013, Section 10.6) we obtain the line to continuum equivalent width. For the H30 α transition and assuming $T_e = 7000$ K, this width is 104.044 MHz or 134.504 km s⁻¹.

Therefore, assuming optically thin conditions and considering that the line is well fitted by a Gaussian (which means we can ignore to a first approximation pressure and opacity broadening), the line peak to continuum ratio for a 49.5 ± 0.3 km s⁻¹ width H30 α line is

$$\frac{134.504 \text{ km s}^{-1}}{\sqrt{\pi/\log(16)} 49.5 \text{ km s}^{-1}} = 2.55 .$$

Therefore, the expected free-free contribution to the continuum is $46.7 \text{ K}/2.55 = 18.3 \text{ K}$.

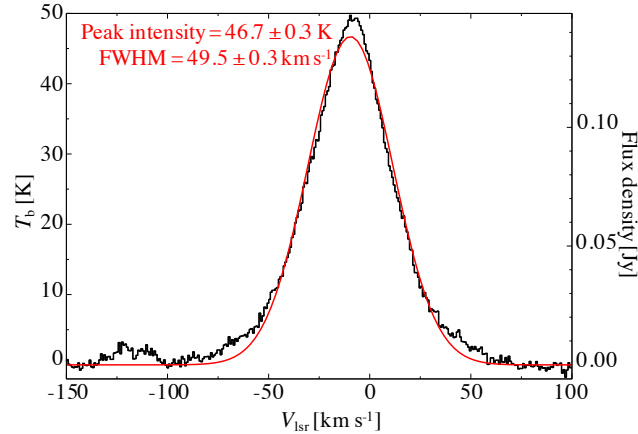


Figure 12. Spectra of H30 α toward Core A. Red line indicates the result of a Gaussian fitting.

B. MODEL RESULTS OF H₂CO

We investigate main formation pathways of H₂CO using the results of Taniguchi et al. (2019) with the Nautilus (Ruaud et al. 2016). The details of this model were described in Taniguchi et al. (2019). The gas density (n_{H}) increases from 10^4 to 10^7 cm⁻³. In order to investigate the temperature dependence in detail, we use results of the 3-phase (gas, dust surface, and bulk of ice mantle) and slow warm-up (1×10^6 yr) model.

Figure 13 represents the time evolution of H₂CO from a starless core to the hot core phase through the warm-up phase. The upper panel of Figure 13 shows the time evolution of gas-phase H₂CO abundance together with the temperature profile. The lower panel shows the production rates of the main formation pathways of H₂CO together with the temperature profile.

During the low-temperature (10 K) starless core stage, the gas-phase reaction between CH₃ and oxygen atom (O) is the main formation route of H₂CO. After the gas density reaches 10^7 cm⁻³ and the temperature starts to increase, the following reaction contributes to the gas-phase H₂CO formation:



This reaction efficiently works before the temperature reaches at 25 K. After the temperature rises above ~ 50 K, the thermal evaporation of H₂CO, which is formed by successive hydrogenation reactions of CO molecules on dust surfaces, is the most efficient route.

REFERENCES

- Belloche, A., Garrod, R. T., Müller, H. S. P., et al. 2014, *Science*, 345, 1584
- Belloche, A., Müller, H. S. P., Garrod, R. T., et al. 2016, *A&A*, 587, A91
- Beltrán, M. T., Cesaroni, R., Neri, R., et al. 2011, *A&A*, 525, A151
- Bonfand, M., Belloche, A., Garrod, R. T., et al. 2019, *A&A*, 628, A27
- Bonfand, M., Belloche, A., Menten, K. M., et al. 2017, *A&A*, 604, A60
- Caux, E., Bottinelli, S., Vastel, C., et al. 2011, *The Molecular Universe*, 120
- Cesaroni, R., Sánchez-Monge, Á., Beltrán, M. T., et al. 2017, *A&A*, 602, A59
- Esplugues, G. B., Viti, S., Goicoechea, J. R., et al. 2014, *A&A*, 567, A95
- Feng, S., Beuther, H., Henning, T., et al. 2015, *A&A*, 581, A71
- Friedel, D. N., & Widicus Weaver, S. L. 2012, *ApJS*, 201, 17
- Furuya, R. S., Cesaroni, R., & Shinnaga, H. 2011, *A&A*, 525, A72
- Garrod, R. T. 2013, *ApJ*, 765, 60
- Gieser, C., Semenov, D., Beuther, H., et al. 2019, *A&A*, 631, A142
- Guzmán, A. E., Garay, G., & Brooks, K. J. 2010, *ApJ*, 725, 734
- Guzmán, A. E., Garay, G., Brooks, K. J., et al. 2011, *ApJ*, 736, 150

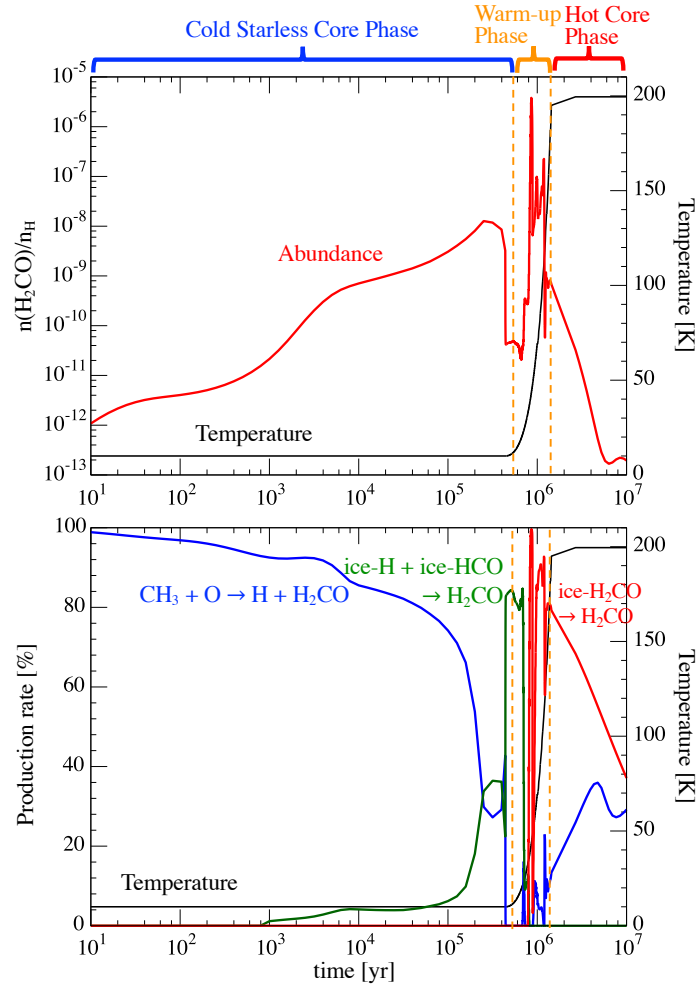


Figure 13. Time dependences of the gas-phase H_2CO abundance (upper panel) and fractions of its main formation pathway (lower panel). Black lines indicate the time dependence of the temperature.

Guzmán, A. E., Garay, G., Rodríguez, L. F., et al. 2014, *ApJ*, 796, 117

Guzmán, A. E., Guzmán, V. V., Garay, G., et al. 2018, *ApJS*, 236, 45

Herbst, E., & van Dishoeck, E. F. 2009, *ARA&A*, 47, 427

Kauffmann, J., Bertoldi, F., Bourke, T. L., et al. 2008, *A&A*, 487, 993

Lumsden, S. L., Hoare, M. G., Urquhart, J. S., et al. 2013, *ApJS*, 208, 11

McMullin, J. P., Waters, B., Schiebel, D., et al. 2007, *Astronomical Data Analysis Software and Systems XVI*, 127

Mottram, J. C., Hoare, M. G., Lumsden, S. L., et al. 2007, *A&A*, 476, 1019

Müller, H. S. P., Schlöder, F., Stutzki, J., & Winnewisser, G. 2005, *Journal of Molecular Structure*, 742, 215

Öberg, K. I., Garrod, R. T., van Dishoeck, E. F., et al. 2009, *A&A*, 504, 891

Pagani, L., Bergin, E., Goldsmith, P. F., et al. 2019, *A&A*, 624, L5

Pickett, H. M., Poynter, R. L., Cohen, E. A., et al. 1998, *JQSRT*, 60, 883

Planck Collaboration, Ade, P. A. R., Aghanim, N., et al. 2011, *A&A*, 536, A23

Riaz, B., Thi, W.-F., & Caselli, P. 2018, *MNRAS*, 481, 4662

Ruaud, M., Wakelam, V., & Hersant, F. 2016, *MNRAS*, 459, 3756

Sadavoy, S. I., Di Francesco, J., Johnstone, D., et al. 2013, *ApJ*, 767, 126

Sewilo, M., Charnley, S. B., Schilke, P., et al. 2019, *ACS Earth and Space Chemistry*, 3, 2088

Skrutskie, M. F., Cutri, R. M., Stiening, R., et al. 2006, *AJ*, 131, 1163

Taniguchi, K., Herbst, E., Caselli, P., et al. 2019, *ApJ*, 881, 57

- Taniguchi, K., Miyamoto, Y., Saito, M., et al. 2018a, *ApJ*, 866, 32
- Taniguchi, K., Plunkett, A., Herbst, E., et al. 2020, *MNRAS*, 493, 2395
- Taniguchi, K., Saito, M., Hirota, T., et al. 2017, *ApJ*, 844, 68
- Taniguchi, K., Saito, M., Majumdar, L., et al. 2018b, *ApJ*, 866, 150
- Tercero, B., Cuadrado, S., López, A., et al. 2018, *A&A*, 620, L6
- van der Tak, F. F. S., Boonman, A. M. S., Braakman, R., et al. 2003, *A&A*, 412, 133
- Vidal, T. H. G., Loison, J.-C., Jaziri, A. Y., et al. 2017, *MNRAS*, 469, 435
- Widicus Weaver, S. L., & Friedel, D. N. 2012, *ApJS*, 201, 16
- Wilson, T. L., Rohlfs, K., & Hüttemeister, S. 2013, *Tools of Radio Astronomy; Astronomy and Astrophysics Library*. ISBN 978-3-642-39949-7. Springer-Verlag Berlin Heidelberg